An integrated dynamic analysis method for simulating installation of single blades for wind turbines

Yuna Zhao [a,c], Zhengshun Cheng [a,b,c,*], Peter Christian Sandvik [d], Zhen Gao [a,b,c], Torgeir Moan [a,b,c]

[a] Centre for Autonomous Marine Operations and Systems (AMOS), NTNU, NO-7491, Trondheim, Norway
[b] Centre for Ship and Ocean Structures (CeSOS), NTNU, NO-7491, Trondheim, Norway
[c] Department of Marine Technology, NTNU, NO-7491, Trondheim, Norway
[d] PC Sandvik Marine, Trondheim, Norway

ARTICLE INFO

ABSTRACT

Installation of blades for wind turbines is challenging due to large lifting height and high precision. Assessment of blade dynamic responses during installation needs advanced simulation tools which are limited at present. This paper aims at developing an integrated simulation tool SIMO-Aero for single blade installation for both onshore and offshore wind turbines. Based on the cross-flow principle, the aerodynamic model is established by accounting for the effect of wind turbulence and dynamic stall. Then it is coupled with SIMO to achieve the integrated simulation tool SIMO-Aero which can account for blade aerodynamics, vessel hydrodynamics and system mechanical couplings. The aerodynamic code is verified by code-to-code comparisons with HAWC2. Furthermore, SIMO-Aero is applied in case studies on the wind-induced dynamic responses of a DTU 10 MW blade during installation using a jack-up crane vessel which is assumed to be rigid, including the crane, and rigidly fixed to the seabed. The characteristics of system dynamic responses prior to mating the blade onto the hub are studied. It is shown that the blade motions are dominated by the pendulum motion. Critical parameters of the installation process are identified. The extreme responses of critical parameters are further studied under turbulent winds and wind gusts.

1. Introduction

In recent years, air pollution and global warming have become important issues to the world, leading to an urgent need of clean, renewable and reliable energy sources such as wind energy. The wind industry has grown significantly in the last decades. The global cumulative installed wind capacity reached 487GW by the end of 2016, which includes about 14.4GW installed offshore (Global Wind Energy Council, 2017). At the same time, the size of wind turbines also increases fast. In 2016, 8MW wind turbines were successfully installed at Burbo Bank offshore wind farm (DONG energy, 2016). The trend towards larger turbine size leads to larger blade size, higher installation height and increased sensitivity to wind condition (and also wave condition for offshore turbines), which adds difficulties to the installation of turbine components, especially the blades.

The three most commonly used methods for blade installation are respectively single blade installation, bunny ear and whole rotor lift

(Uraz, 2011). Among those, single blade installation is most frequently used for offshore installation in recent years, due to small deck space requirement and flexible blade orientations during installation (Ahn et al., 2017). During the installation process, the blade is lifted and installed in a feathered position, which is kept during the whole installation operation (Kuijken, 2015; Siemens, 2014b; High Wind NV, 2015). As shown in Fig. 1, the single blade can be installed in various orientations such as horizontal, vertical or even inclined. For inclined-blade installation, longer crane boom is required as the blade needs to be lifted higher than the hub height. The vertical-orientated installation needs to rotate the blade prior to installation since it is horizontally stored on the vessel deck, which makes the process more complex. The horizontal orientation installation is most preferred since no rotation of blade is required. Besides, installations of blades for offshore wind turbines are commonly conducted by jack-up crane vessels rather than floating ones since they provide a very stable working platform.

Wind condition is the one of the main constraints for blade installa-

* Corresponding author. Department of Marine Technology, NTNU, NO-7491, Trondheim, Norway.
  E-mail addresses: yuna.zhao@ntnu.no (Y. Zhao), zhengshun.cheng@ntnu.no (Z. Cheng).

Fig. 1. Single blade installation of offshore wind turbine blades with various orientations.

(a) Horizontal mounting (Siemens, 2014b)

(b) Vertical mounting (Liftra, 2012)

(c) Inclined mounting (Liftra, 2012)

tion wind turbines since it directly affects the waiting time for suitable weather window, which causes large economic cost. By now, most of the lifting equipment for single blade installation can operate under wind speed of 10 m/s. There are also advanced installation equipment such as Blade Dragon (Liftra, 2012), B75 lifting yoke (Siemens, 2014a) and Boom Lock (High Wind NV, 2015). The Blade Dragon, which is shown in Fig. 1(b)~1(c), has a remote control system and can install blades with all orientations. It claims that installation of blades can take place at a speed below 12m/s. The B75 lifting yoke in Fig. 2(a) is claimed to be capable of installing blades in average wind speed up to 14m/s. It has automatic sling connection and can actively yaw itself to adjust the blade position during installation. The Boom Lock in Fig. 2(b) is a system mounted on crane boom to control the blade movement, which is claimed to allow installation of blades in average wind speed up to 15m/s.

Since the installation of blades for wind turbines is challenging, it is of importance to establish and use advanced numerical simulation tools to study the dynamic response of blade during installation. The dynamic response could be further used to predict the available weather windows if the installation criteria are known.

However, so far a limited number of studies on blade installations for wind turbines have been published. Some studies focus on the aerodynamic modeling of blades during installation or under standstill conditions. The characteristics of aerodynamic loads acting on a blade under installation conditions are quite different from a blade of an operating wind turbine. Wang et al. (2014) studied the hoisting forces on a wind turbine blade during installation using computational fluid dynamics (CFD) under constant wind conditions. Gaunaa et al. (2016) assessed the performance of cross-flow principle on the DTU 10MW reference blade in standstill situations using extensive three-dimensional CFD calculations. The authors concluded that the cross-flow principle gives a good estimation of aerodynamic loading when the blade pitch angle is within $\left[-50° \quad 50°\right]$. These CFD analyses specialize in accurate estimation of aerodynamic loads based on solving Navier-Stokes equations. However, they require significant computational efforts and cost. Thus, it is not suitable for simulation of marine operations.

Others focus on the installation process of blades for wind turbines. Wang et al. (2012) studied the hoisting force of a 1.5MW wind turbine

(a)   (b)

Fig. 2. Advanced equipment for installation of blades for offshore wind turbines: (a) B75 lifting yoke (Siemens, 2014a); (b) Boom Lock (High Wind NV, 2015).

rotor using Bladed (GL Garrad Hassan, 2010). Gaunaa et al. (2014) proposed a general scaling method regarding the mean and standard deviations of aerodynamic loads on a single blade in yawed and pitched wind conditions. Kuijken (2015) examined possible ways to improve single blade installation in higher wind speed using HAWC2 (Larsen and Hansen, 2015). However, Bladed and HAWC2 are designed to calculate time-domain responses for wind turbine systems which are already in operation. Moreover, they cannot provide accurate models for mechanical couplings such as lift wires, slings and tugger lines, which are of great importance in the modeling of blade installation for wind turbines. Therefore, more sophisticated simulation tools for analysis of blade installation for wind turbines should be developed.

In this paper, a novel coupled simulation tool SIMO-Aero is developed for wind turbine blade installation in which an aerodynamic code is fully coupled with SIMO, a software specialized in numerical simulation of marine operations. The aerodynamic modeling is firstly described considering the effect of turbulent wind inflow and dynamic stall. Then the aerodynamic code is coupled with SIMO to establish the integrated simulation tool SIMO-Aero. SIMO-Aero is similar to SIMO-Riflex-Aerodyn (Kvittem et al., 2012) and SIMO-Riflex-AC (Cheng et al., 2016) which are fully coupled simulation tools integrating an external aerodynamic model with SIMO and Riflex for time-domain simulations of offshore wind turbine systems during installation. The SIMO-Aero proposed in this paper can be used to study the dynamic responses of single-blade-installation system for both onshore and offshore installations. Moreover, it has great potential to develop more efficient methods for installation or removal of blades for offshore wind turbines using a floating crane vessel.

The aerodynamic code in the integrated simulation tool is verified against HAWC2 results using the DTU 10MW reference wind turbine blade (Bak et al., 2013). The developed simulation tool is applied in a series of load cases to study the characteristics of wind-induced dynamic responses of the blade installation system in turbulent winds and extreme operating gust winds.

2. Aerodynamic modeling

In this section, the aerodynamic modeling of a single blade is presented based on the cross-flow principle. Before going into details of the aerodynamic model, the coordinate systems used in the modeling are clearly defined.

2.1. Reference frame

As shown in Fig. 3, three coordinate systems were used, i.e., the global coordinate system $OXYZ$, body-fixed coordinate system for the blade $oxyz$ and local airfoil (blade cross-section) coordinate system $o_c x_c y_c z_c$, which are all right-handed coordinate systems. The origin o of the blade body-fixed coordinate is located at the blade center of gravity (COG). The y-axis is in the spanwise direction and x-axis is positive towards the trialling edge while z-axis follows the right-hand rule. The instantaneous rotational motions of the blade around X, Y and Z axis are respectively roll(ϕ), pitch(θ) and yaw(ψ). When ϕ, θ and ψ are all zero,
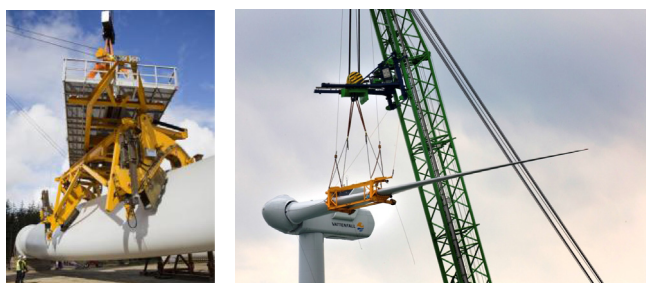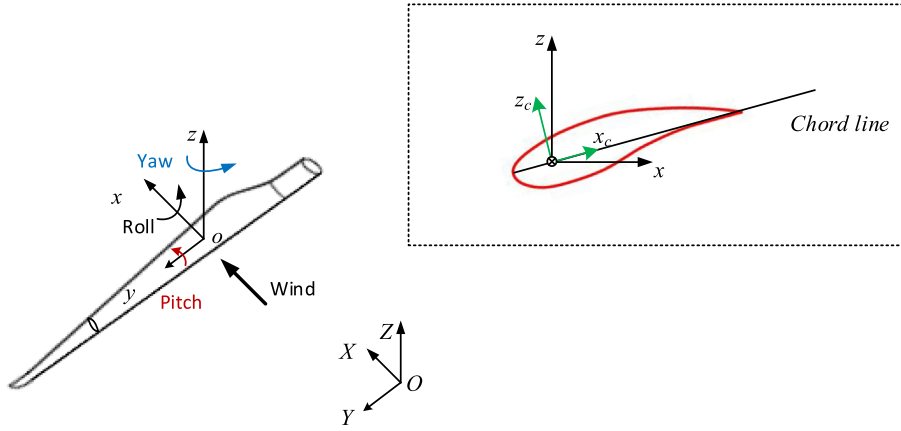
Fig. 3. Definition of coordinate systems.

oxyz parallels with the global coordinate *OXYZ*. The y_c-axis of the local airfoil coordinate coincides with the y-axis while the x_c-axis is along the chord line.

Given a vector represented by $\mathbf{L}_G$ in the global coordinate system, its representation in the blade body-fixed coordinate system is:

$$\mathbf{L}_b = \mathbf{T}_{GB}\mathbf{L}_G \tag{1}$$

Furthermore, the representation of L_b in the local airfoil coordinate system is:

$$\mathbf{L}_c = \mathbf{T}_{BC}\mathbf{L}_b \tag{2}$$

where $\mathbf{T}_{GB}$ and $\mathbf{T}_{BC}$ are the coordinate transformation matrix. The $\mathbf{T}_{GB}$ is a function of instantaneous blade rotational motion ϕ, θ, ψ while $\mathbf{T}_{BC}$ is a function of structural twist angle of blade local cross-sections. The transformation matrix from the global coordinate to the local airfoil coordinate $\mathbf{T}_{GC}$ is:

$$\mathbf{T}_{GC} = \mathbf{T}_{BC}\mathbf{T}_{GB} \tag{3}$$

2.2. Cross-flow principle

In the aerodynamic force calculation, the blade is divided into a number of elements. For each element, the calculation of aerodynamic loads is based on the cross-flow principle (Horner, 1965; Hoerner and Borst, 1985), which has been widely used in wind energy industry. In the cross-flow principle, the inflow velocity normal to the cross section is neglected, as shown in Fig. 4. Thus, the component of relative inflow velocity $\mathbf{V}_{A,i}$ on y_c axis is neglected, i.e.:

$$\mathbf{V}_{rel} = [V_{A,i,xc} \quad 0 \quad V_{A,i,zc}]^T \tag{4}$$

where $V_{A,i,xc}$ and $V_{A,i,zc}$ are respectively the projection of $\mathbf{V}_{A,i}$ on axis x_c and y_c. This principle is applicable for calculation of aerodynamic forces
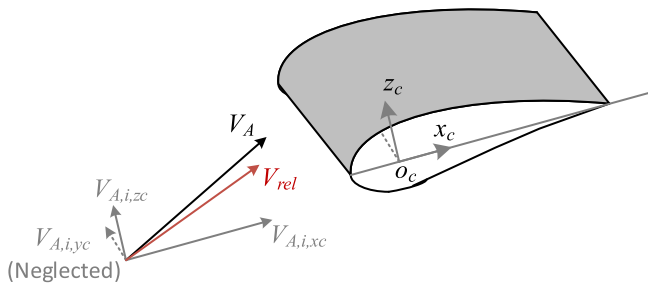
Fig. 4. Illustration of cross-flow principle: $\mathbf{V}_{A,i} = [V_{A,i,xc} \quad V_{A,i,yc} \quad V_{A,i,zc}]^T$

on a wind turbine blade, where the local blade element suits a 2D approximation.

The characteristics of $\mathbf{V}_{rel}$ for an element on a lifted blade are quite different from that on a rotating one. For an element a rotating blade, the large rotational speed has a significant contribution to $\mathbf{V}_{rel}$. However, the $\mathbf{V}_{rel}$ for an element on a lifted blade is mainly from the inflow wind velocity. It leads to significant discrepancies in aerodynamic loading on the whole blade. The overall difference in aerodynamic load between a lifted blade and a rotating blade is further discussed in Section 6.1.

2.3. Calculation of aerodynamic forces

Fig. 5 shows a flow diagram for calculating the aerodynamic load on a lifted blade. The instantaneous displacement and velocity of the blade are respectively $\mathbf{X}_B\left([x(t) \; y(t) \; z(t) \; \theta(t) \; \psi(t)]^T\right)$ and $\mathbf{V}_B\left([v_x(t) \; v_y(t) \; v_z(t) \; v_\phi(t) \; v_\theta(t) \; v_\psi(t)]^T\right)$ at each time step. The whole blade is divided into a number of elements. The total force on the blade is the sum of those on all elements.

For each element, its instantaneous position and velocity in the global coordinate system is calculated:

$$\mathbf{X}_i = \mathbf{X}_B^{1\sim3} + \mathbf{T}_{GB}^T(t)\mathbf{r}_{i,b} \tag{5}$$

$$\mathbf{V}_i = \mathbf{V}_B^{1\sim3} + \mathbf{V}_B^{4\sim6} \times \left[\mathbf{T}_{GB}^T(t)\mathbf{r}_{i,b}\right] \tag{6}$$

where $\mathbf{X}_i = [x_i(t) \quad y_i(t) \quad z_i(t)]^T$ and $\mathbf{V}_i = [v_{x,i}(t) \quad v_{y,i}(t) \quad v_{z,i}(t)]^T$; $\mathbf{r}_{i,b}$ is the position vector of element i in the blade body-fixed coordinate. Based on the global position of the ith element, the wind inflow velocity at this element could be obtained, i.e., $\mathbf{V}_{WG,i}$. The corresponding relative inflow velocity $\mathbf{V}_{A,i}$ in the local airfoil coordinate can be derived from:

$$\mathbf{V}_{A,i} = \mathbf{T}_{GC,i}(\mathbf{V}_{WG,i} - \mathbf{V}_i + \mathbf{V}_{IG,i}) \tag{7}$$

The $\mathbf{V}_{IG}$ is the wake induced velocity. It is significant for a rotating blade with large rotational speed. However, it has marginal influence for blades during installation because the blade motion is very small. Therefore, it is neglected here.

Afterwards, the relative velocity $\mathbf{V}_{rel}$ used for further aerodynamic calculation is obtained using $\mathbf{V}_{A,i}$ based on the cross-flow principle, which was discussed in detail in Section 2.2. Then, the angle of attack α is determined. It is used to calculate the lift coefficient C_L and drag coefficient C_D based on a 2D look-up table. The table gives the relationship between C_L, C_D and α. Based on the calculated C_L and C_D coefficients for each element, the aerodynamic lift, drag force are calculated. Furthermore, the aerodynamic forces on the whole blade are obtained as the sum of those on all elements. The total aerodynamic forces are given in the global coordinate system at blade COG.
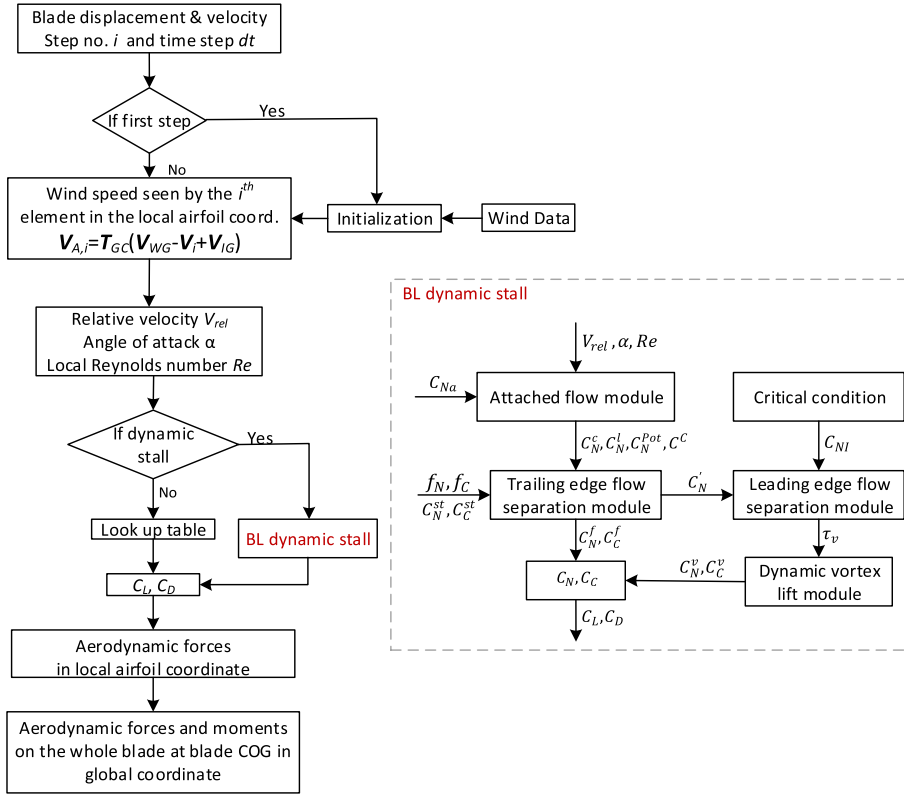
Moreover, there is an option to include dynamic stall effect before the table look-up. The Beddoes-Leishman dynamic stall model is used, which is explained in the next section.

2.4. Beddoes-Leishman stall model

The Beddoes-Leishman dynamic stall model was originally proposed by Leishman and Beddoes (1989) for helicopter aerodynamics. Later, Gupta and Leishman (2006) adapted it for application in wind turbine aerodynamics. As shown on the right side of Fig. 5, there are three parts in the Beddoes-Leishman dynamic stall model, i.e., unsteady attached flow, unsteady separated flow and dynamic vortex lift.

In the unsteady attached flow regime, the aerodynamic loading consists of a circulatory and an impulsive part. The circulatory component is due to the change of angle of attack while the impulsive component is related to the change rate of α and pitch moment. Furthermore, the attached flow results are modified due to flow separation on the low-pressure side of the airfoil, including leading edge and trailing edge separations. The final part of the model is the vortex build-up and shedding. The vortex lift contribution is empirically modeled as an excess circulation in the vicinity of the airfoil using the difference between the normal force coefficient C_N from attached flow and separated flow. The total loading on the airfoil is the sum of the aforementioned components.

2.5. Inflow wind

The developed simulation tool can account for steady wind, turbulent wind and gust wind. The steady wind is constant in time and space. The turbulent wind is described by the IEC Kaimal Model (IEC, 2005). For the turbulent wind, the three-dimensional full-field wind file is generated by using the NREL's TurbSim program (Jonkman, 2009). The extreme operating gust wind is defined according to IEC 6400-1 (IEC, 2005).

The effects of wind shear is considered in the inflow wind. The wind shear effect is described by the power law wind profile, i.e.:

$$V(z) = V\left(z_{ref}\right)\left(\frac{z}{z_{ref}}\right)^{\alpha_s} \tag{8}$$

where $V(z)$ is the wind speed at height z while $V(z_{ref})$ is the wind speed at reference height z, which is normally the hub height. In addition, α_s is the wind shear exponent (IEC, 2009).

The wind yaw angle ψ_W is defined as the angle between the wind inflow direction and the global X-axis in OXY plane. It is positive in the anticlockwise direction. As shown in Fig. 6, the wind flows along the positive global X axis when ψ_W is zero.

3. Development of the integrated simulation tool

The developed aerodynamic code is coupled with SIMO (MARINTEK, 2015a, b) to formulate the integrated simulation tool SIMO-Aero for blade installation. SIMO is widely used in time-domain simulations of marine operations in the offshore oil&gas and renewable energy industries. It could be used to simulate dynamic loads and responses for onshore foundations and offshore jack-up crane vessels or floating vessels. The coupled SIMO-Aero code could account for aerodynamics of the installed blade, hydrodynamics of the installation vessel and mechanical couplings between bodies in the multi-body system.
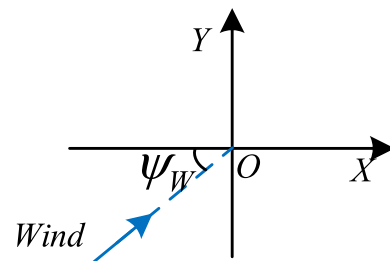

Fig. 6. Illustration of wind inflow direction.

The SIMO-Aero code developed in this paper is a fully coupled code. As shown in Fig. 7, the instantaneous blade displacement and velocity in the global coordinate system is calculated by SIMO at each time step. The instantaneous displacement is used to update the transformation matrix from global to local blade element coordinate systems. Then the blade velocity and wind inflow velocity in the global coordinate system are transferred into the local blade element coordinate system, to update the relative velocity seen by the local blade element and the angle of attack. The corresponding lift and drag coefficients are determined from a look-up table, and are used to estimate the lift and drag forces in the local blade element coordinate system. These aerodynamic forces are then transferred into the global coordinate system, and are sent back to SIMO to calculate the blade displacement and velocity for the next time step.

Fig. 8 shows the modeling of external loads and internal coupling for the blade installation system. The system for blade installation usually consists of a crane vessel, a hook, a yoke and the blade to be installed. The hook is connected to the crane via the lift wire. Four slings spread down from the hook to the yoke which holds the blade. The blade and the yoke are modeled as one rigid body denoted by BY. Two horizontal tugger lines run from the yoke to the crane boom in order to control the blade motions.

In the present paper, the coupled SIMO-Aero code was applied in case studies with focus on the wind-induced responses of the blade. A jack-up crane vessel which is assumed to be rigid and rigidly fixed to the seabed is used. The wave load, hydrostatic loads and current loads are all not considered for the jack-up crane vessel.

3.1. Aerodynamic model

The aerodynamic model is extensively described in Section 2. It is based on the cross-flow principle and accounts for the effect of turbulence and dynamic stall. However, there are still limitations in the aerodynamic model. The dynamic inflow effect, the wind loads on yoke and influence of yoke geometry on the flow field are assumed to be insignificant and not included. For the case study presented later, a straight blade is considered. Besides, the blade is assumed to be rigid. Gaunaa et al. (2014) studied the importance of structural flexibility for a wind turbine blade during installation using the DTU 10MW blade. It was found that the influence of structural flexibility is negligible as long as the natural frequency of blade rigid body motion is below 2.51 rad/s (0.4 Hz). The results in Section 7.1 show that the natural frequency of blade rigid motion is 0.5 rad/s, which is well below 2.51 rad/s. Thus, the blade flexibility has minor effect on the dynamic response of the blade during the installation phase.

3.2. Mechanical coupling model

The bodies involved in the blade installation system are coupled with each other via lift wire, slings or tugger lines. The coupling forces in the wires are modeled as linear spring forces (zero compression):

$$T = k\Delta L \quad (T > 0) \tag{9}$$

where T is the wire tension and ΔL is the wire elongation. Besides, k is the axial stiffness of the wire, which is given by:

$$\frac{1}{k} = \frac{L}{EA} + \frac{1}{k_0} \tag{10}$$

where L and A are respectively the length and cross-sectional area of the wire, E the modulus elasticity of the material of the wire and $1/k_0$ the connection flexibility.

4. System description

Since jack-up crane vessels are most commonly used for blade installations of offshore wind turbines, a jack-up crane vessel is used in the following case studies, as shown in Fig. 9.

The blade used in this study is the DTU 10MW reference wind turbine blade (Bak et al., 2013). The hub height is 119 m above the mean sea surface. The blade is considered to be straight, which is 86.37 m long and weighs about 42 tons. The blade COG is located 26.2 m from its root. The blade is divided into 55 elements during the calculation of aerodynamic loads. The corresponding chord length, twist angle, thickness and airfoil coefficients at each blade element are interpolated based on those described by Bak et al. (2013).

A yoke weighting 47 tons is placed around the blade COG to hold the blade. Two horizontal tugger lines are deployed from the yoke to the crane structure. Both tugger lines are 3 m long and have an arm length of 10 m, as shown in Fig. 9. Table 1 is a summary of the system properties.

The detailed wire properties in the system are presented in Table 2. The crane wire is a typical metal wire rope with diameter of 60 mm (Lankhorst ropes, 2013). The flexibility of the lift wire is due to the deformation of the crane boom and wires from crane tip to crane winch. The slings have a diameter of 30 mm while the diameter of the tugger lines is 5 mm. In addition, material damping in wire is included in the model, which is about 1% of the wire stiffness according to the SIMO Theory Manual (MARINTEK, 2015a).

4.1. Eigenvalue analysis

Eigenvalue analysis is conducted to evaluate the eigen periods of rigid body motions of the hook, blade and yoke. In the numerical model, the blade and yoke are modeled as one body, which is denoted by BY. The eigen periods and modes are obtained by solving Eq. (11):

$$\left[-\omega^2(\mathbf{M} + \mathbf{A}) + \mathbf{K} \right] \cdot \mathbf{X} = 0 \tag{11}$$

where $\mathbf{M}$, $\mathbf{A}$ and $\mathbf{K}$ are the mass, added mass and restoring matrix of the BY and hook. Since they are in air, the added mass matrix $\mathbf{A}$ is zero. In addition, the restoring matrix $\mathbf{K}$ mainly comes from the gravity of involved bodies, lift wire, slings and tugger lines.

As shown in Table 3, the BY and hook coupled motions have 9 eigen modes. The dominated motion(s) of each eigen mode is emphasized in bold. The 1st mode has the largest eigen period 13.63s, corresponding to the system pendulum motion in the blade local $y_b z_b$ plane shown in Fig. 9. The 2nd is dominated by the yaw motion of the BY. The 3rd mode is a
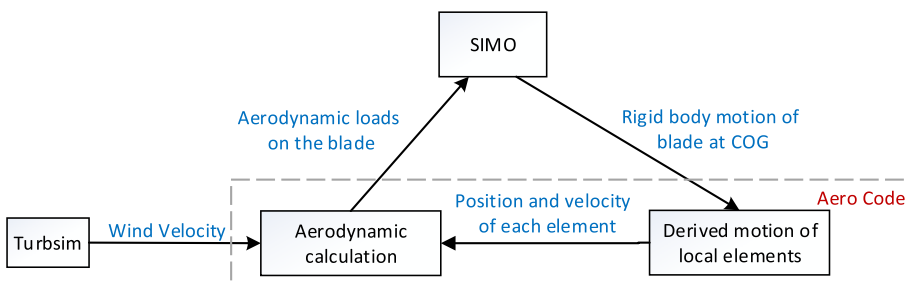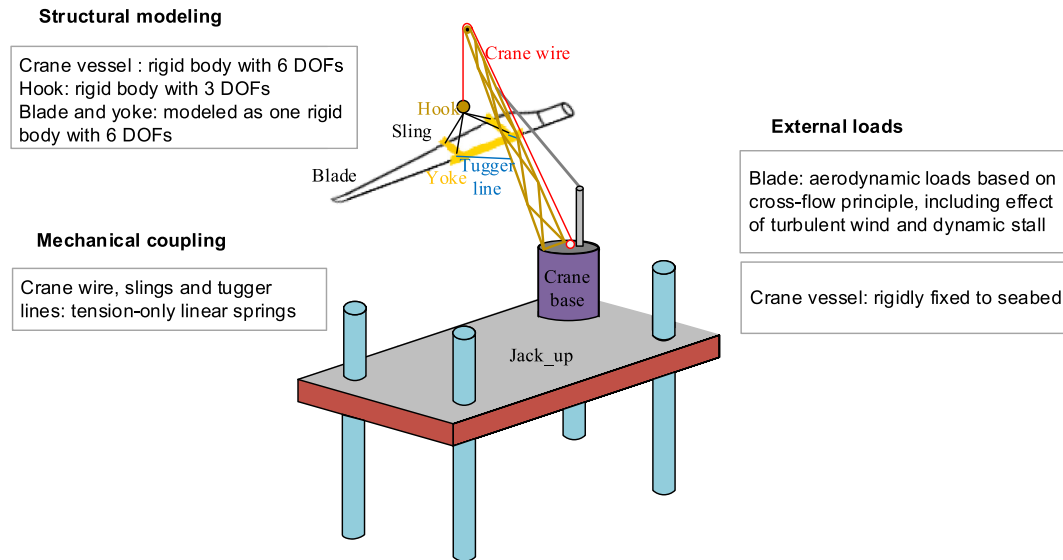
Fig. 7. Overview of the coupled simulation tool.

Structural modeling

Crane vessel : rigid body with 6 DOFs
Hook: rigid body with 3 DOFs
Blade and yoke: modeled as one rigid body with 6 DOFs

Mechanical coupling

Crane wire, slings and tugger lines: tension-only linear springs

External loads

Blade: aerodynamic loads based on cross-flow principle, including effect of turbulent wind and dynamic stall

Crane vessel: rigidly fixed to seabed

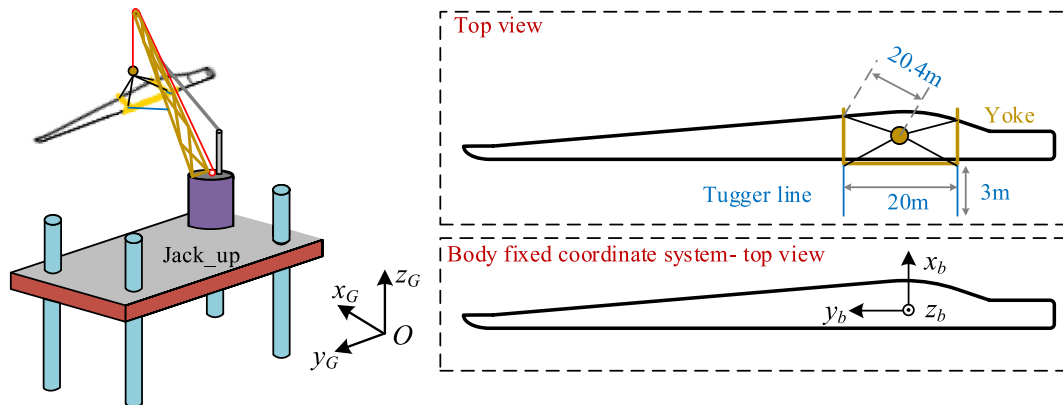**Fig. 8.** Illustration of overall modeling for offshore blade installation system.

Fig. 9. Illustration of blade installation system.

Table 1
Main properties of the blade lifting system.

Parameter	Value	Unit
Hook mass	10	tons
Yoke mass	47	tons
Blade mass	41.67	tons
Blade length	86.37	m
Installation height	119	m
Tugger line arm length	10	m

Table 2
Main parameters of the mechanical coupling.

Parameter	Unit	Lift wire	Slings	Tugger lines
L	[m]	4.7	20.4	3.0
EA/L	[kN/m]	1.06e5	5.87e3	1.17e3
k_0	[kN/m]	5.0e3	–	–
Damping	[kNs/m]	1.06e3	5.87e1	1.17e1

combination of transnational motions in the horizontal plane and rotational motion in the vertical plane. The eigen periods of these two modes are much shorter due to the influence of the tugger lines. The last 6 modes have short natural periods, which are below 3s. The first mode is

the most important for the dynamics of the system, as demonstrated by the spectral analysis of blade motion in Section 7.1.

5. Load cases and environmental conditions

A series of load cases are defined for code verification and time domain simulations, as given in Tables 4 and 5. It should be noted that these load cases are not from design codes, but are only chosen for the numerical study in this paper. However, the largest turbulence intensity 15.72% in the load cases is chosen according to the design class C in IEC 6400-1 (IEC, 2005).

Load case LC1 is the steady wind case, which is used to verify the aerodynamic code.

In load case LC2, turbulent wind is applied. It is used to demonstrate the necessity of using an advanced aerodynamic model and how much inaccuracy a simplified aerodynamic model might cause as discussed in Section 6. The simplification made means that blade velocity is neglected in the calculation of aerodynamic loads.

Load case LC3 is a turbulent wind case with varying turbulence intensity T_I. LC3 is designed to study the characteristics of the blade installation system under turbulent wind condition, including global motion of the blade, aerodynamic loads acting on the blade and tension in crane wire and tugger lines.

Table 3
Eigen modes and natural periods for BY (blade and yoke) and hook rigid body motions.

Mode		1	2	3	4	5	6	7	8	9
$x_{BY,1}$	[m]	0.00	0.00	0.00	0.13	−0.09	0.12	0.00	0.01	0.00
$x_{BY,2}$	[m]	0.37	**0.70**	−0.14	0.00	0.00	0.00	−0.11	0.00	0.00
$x_{BY,3}$	[m]	0.00	0.00	0.00	−0.01	0.03	**1.00**	0.00	0.00	−0.09
$x_{BY,4}$	[deg]	**1.00**	**−0.94**	0.31	0.00	0.00	0.00	0.15	0.00	0.00
$x_{BY,5}$	[deg]	0.00	0.00	0.00	**−1.00**	**−1.00**	0.35	0.00	**−1.00**	−0.02
$x_{BY,6}$	[deg]	0.10	**−0.84**	**−1.00**	0.00	0.00	0.00	0.00	0.00	0.00
$x_{H,1}$	[m]	0.00	0.00	0.00	−0.19	−0.51	0.40	0.00	0.02	0.04
$x_{H,2}$	[m]	0.01	**1.00**	−0.26	0.00	0.00	0.00	**1.00**	0.00	0.00
$x_{H,3}$	[m]	0.00	0.00	0.00	0.00	0.05	**0.79**	0.00	0.00	**1.00**
T_n	[sec]	13.63	3.72	3.45	1.59	1.15	0.99	0.24	0.18	0.13

Note: $x_{BY,1} \sim x_{BY,6}$– BY motion in six degrees of freedom; $x_{H,1} \sim x_{H,3}$– translational motions of the hook.

Table 4
Definition of load cases with steady or turbulent wind.

	U_W [m/s]	ψ_W [deg]	T_I [%]	θ_B [deg]	T_S [s]	N_S
LC1	10	[−120∼120]	0	[0 30 45 60 90]	100	1
LC2	10	0	15.72	[0 45]	600	50
LC3	10	0	[1 3 5 7 9 11 13 15.72]	0	600	50
LC4	10	0	[1 3 5 7 9 11 13 15.72]	30	600	50
LC5	10	0	[1 3 5 7 9 11 13 15.72]	45	600	50
LC6	10	[0 15 30 45 60 75]	15.72	0	600	50

Note: U_W– mean wind speed at hub height; ψ_W– wind yaw angle; T_I– inflow wind turbulence intensity; θ_B– blade initial pitch angle; T_S– simulation time of each run; N_S– number of runs for each sub-case.

Table 5
Definition of load cases with gust wind.

	U_W [m/s]	ψ_W [deg]	θ_B [deg]	T_G [s]	T_S [s]	N_S
LC7	10	0	0	10.5	600	1
LC8	10	0	45	10.5	600	1

Note: T_G– duration of gust wind.

Turbulent wind is also used in load cases LC4 and LC5 while their initial blade pitch angles θ_B are different from LC3. The θ_B represents the initial orientation of blade relative to the horizontal plane. LC4 and LC5 are used for comparison against LC3 to analyze the influence of blade pitch angle on two vital parameters during installation system, i.e., the blade root motion and loads in tugger lines.

In load case LC6, the turbulence intensity T_I is constant while the wind inflow angle ψ_W varies from $0°$ to $75°$. The corresponding results show the influence of ψ_W on the extreme responses.

In load case LC1, only one run with duration of 100s is conducted since the blade is fixed and the wind is steady. However, 50 runs are executed for each simulation with duration of 600s in the turbulent wind load cases LC2 ∼ LC6. The reason for using 10min as the simulation time is that the duration of mating the blade onto hub usually takes approximately 10min. Fifty runs are to ensure the robustness of the obtained statistics. Moreover, 500s is used before the turbulent wind starts in each simulation to remove the transient effect due to simulation start up.

Extreme operating gust wind (EOG) represents rapid change in wind speed. It is applied to study the dynamic responses of the blade installation system under sudden transient change of inflow wind speed. Table 5 lists the EOG load cases. Load cases LC7 and LC8 have the same gust wind while their blade pitch angles θ_B are different. The purpose is to study the dynamic response of the blade installation system under extreme operating gust wind and the influence of θ_B on the dynamic responses. The wind speed of an EOG is given as:

$$V(z,t) = \begin{cases} V(z) - 0.37V_{gust}sin(3\pi t/T_G)(1 - cos(2\pi t/T_G)) & \text{for} \quad 0 \leq t \leq_G \\ V(z) & \text{otherwise} \end{cases}$$

(12)

where T_G is the duration of wind gust, i.e. $10.5s$ (IEC, 2005). Besides, V_{gust} is the gust velocity at the hub height, which is determined by the hub height wind speed, etc. In addition, V_z is the wind speed at height z, which is determined by the wind shear effect and wind speed at hub height.

6. Verification of the coupled simulation tool

Verification of the coupled simulation tool is carried out module by module. SIMO has been widely validated and used in the offshore oil&gas and renewable energy industries. Therefore, only verification of the Aero Code is carried out. Code-to-code comparison against HAWC2 is conducted using the DTU 10MW Reference Wind Turbine blade under load case LC1. Fig. 10 show the comparison of lift and drag force. It is shown that the results from the developed code are in good accordance with the HAWC2 results. However, it should be noted that this code-to-code comparison only verifies the aerodynamic code but does not validate the model against experimental data since they are very difficult to obtain.

Fig. 10 reveals the influence of blade pitch angle θ_B ($0° < \theta_B < 90°$) and wind yaw angle ψ_W ($-120° < \psi_W < 120°$) on the blade aerodynamic loads. With the increase of θ_B, the aerodynamic lift force F_z firstly experiences an increasing trend before θ_B reaches $45°$ and then starts to decrease until $\theta_B = 90°$. However, the aerodynamic drag force F_x experiences a consistent increase until $\theta = 90°$. At the mean time, both F_z and F_x scale with the cosine function of ψ_W. The peak value of F_x at $\psi_W = 0°$ is over $30kN$, which is 50% larger than the peak of F_z at the same yaw angle. The roll moment M_x shown in Fig. 11(a) shares the same trend with F_z because it is the integration of lift force along the blade with an arm around the blade COG. Similar to F_D, the yaw moment M_z increases until θ_B reaches $90°$.

6.1. Comparison of aerodynamic force distribution on a lifted blade and a rotating blade

The distribution of aerodynamic forces on a lifted blade is quite different from a rotating one. Fig. 12 compares the lift and drag force distribution on a blade during rotation and lifted condition in LC1. The blade has zero initial pitch angle in both conditions. Besides, the rotating blade has a rotational speed of 8.029 rpm. As shown in Fig. 12, both lift and drag forces for the rotating blade experience an increasing trend towards the tip. The aerodynamic center of the rotating blade stays close to the blade tip. It indicates that the rotational speed plays an important role in the aerodynamic force distribution of a rotating blade. For the lifted blade, the main contribution of the aerodynamic loads comes from the middle and root part of the blade. Thus, the aerodynamic center of a
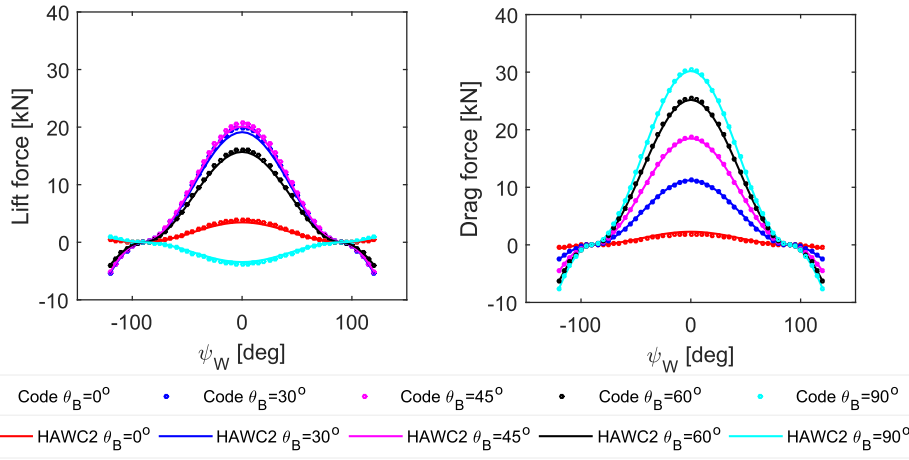
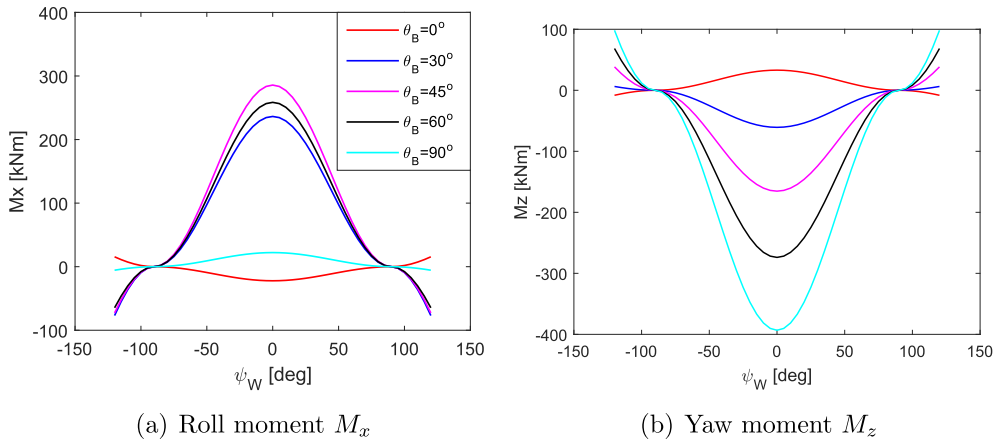**Fig. 10.** Verification of the aero code against HAWC2 in LC1.

Fig. 11. Blade aerodynamic roll and yaw moment calculated from code at different blade pitch angle and wind yaw angle in LC1.
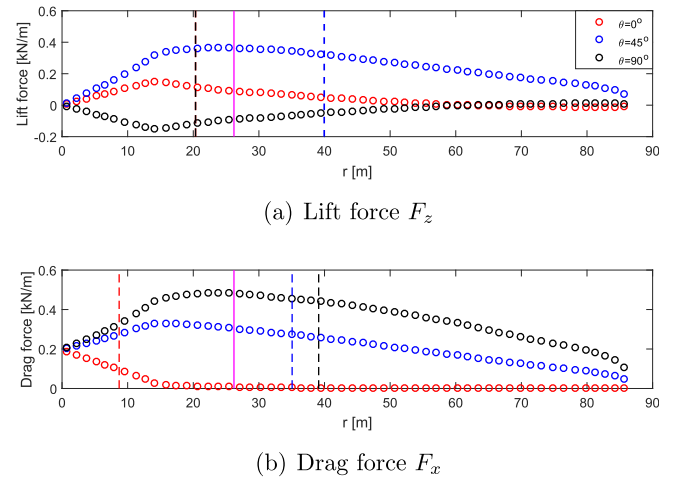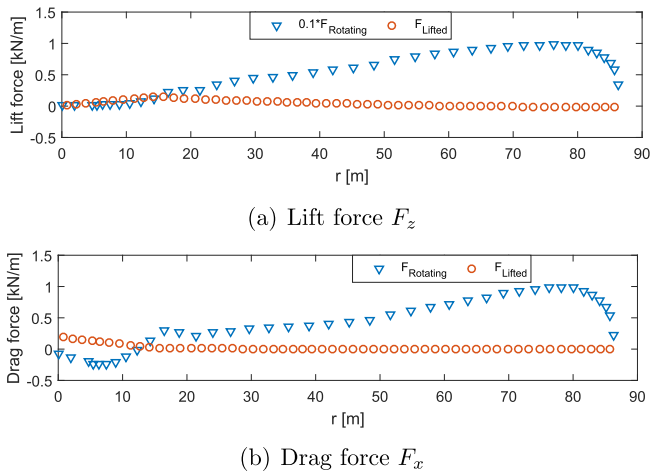
(a) Roll moment M_x

(b) Yaw moment M_z

(a) Lift force F_z

(b) Drag force F_x

Fig. 12. Comparison of distribution of lift and drag forces on a blade under rotating condition and lifted condition in LC1: $\theta_B = 0°$ and blade rotational speed 8.029 rpm.

(a) Lift force F_z

(b) Drag force F_x

Fig. 13. Lift and drag force distribution of a lifted blade in LC1: $\psi_W = 0°$.

lifted blade is located close to the blade root. Compared to the inflow wind velocity, the velocity of a lifted blade is insignificant.

Fig. 13 shows the aerodynamic distribution on a lifted blade with variation of blade pitch angle in LC1. The pink dense line Fig. 13 represents the blade COG while the dotted lines stands for the aerodynamic center at different θ_B. As shown in Fig. 13(a), the aerodynamic center of

lift force for $\theta_B = 0°$ is 20 m from the blade root. Then it moves to around 40 m from root at $\theta_B = 45°$. Afterwards, it moves back towards the blade root as θ_B increases. When the blade pitch angle is $90°$, the aerodynamic center of lift force is the same with zero pitch angle. On the contrary, the aerodynamic center of drag force consistently moves towards blade tip as θ_B increases.

6.2. Influence of blade velocity on the system response

In the current method for calculation of aerodynamic loads, the velocity $\mathbf{V}_i$ at blade elements due to blade motion, i.e., $\mathbf{V}_{MG}$, is taken into consideration, as shown in Eq. (7). Since the blade velocity is small compared with wind inflow velocity, there might be thoughts to neglect the blade velocity (BV) in the aerodynamic load calculation. In this section, the influence of blade velocity in the aerodynamic load calculation is discussed.

- Approach With BV: considering $\mathbf{V}_i$ in the calculation of aerodynamic loads; the relative inflow velocity in the local airfoil coordinate system is:

$$\mathbf{V}_{A,i} = \mathbf{T}_{GC,i}(\mathbf{V}_{WG,i} - \mathbf{V}_i) \tag{13}$$

- Approach Without BV: neglecting $\mathbf{V}_i$ in the calculation of aerodynamic loads; the relative inflow velocity in the local airfoil coordinate system is:

$$\mathbf{V}_{A,i} = \mathbf{T}_{GC,i}\mathbf{V}_i \tag{14}$$

In addition, it should be noted that the instantaneous position of the blade is used in the coordinate transformation matrix $\mathbf{T}_{GC,i}$ in both approaches. Load case LC2 is used in the comparison of these two approaches. The blade roll motion and aerodynamic roll moment on the blade are taken as examples in the comparison.

Figs. 14 and 15 respectively compare the time series and spectra of the blade roll motion and aerodynamic roll moment on the blade calculated based on approach With BV (with consider blade velocity in the calculation of aerodynamic load) and Without BV (without consider blade velocity in the calculation of aerodynamic load) in LC2 with blade initial pitch angle $\theta_B = 0°$. As shown in Fig. 14(a) and (b), neglecting the blade velocity during the calculation of aerodynamic loads leads to a marginal decrease of the amplitude of aerodynamic roll moment M_x at $\omega = 0.46 rad/s$ which is the resonant frequency of roll motion. As a consequence, neglecting the blade velocity leads to significant discrepancies in the blade motion, as shown in Fig. 15(a) and (b). Similar trends are seen in the comparison of these two approaches in LC2 with blade initial pitch angle $\theta_B = 45°$, as shown in Figs. 16 and 17. However, neglecting the blade velocity during the calculation of aerodynamic loads at $\theta_B = 45°$ leads to a much smaller difference in blade roll motion. Because the total aerodynamic roll moment on the blade at $\theta_B = 45°$ is less sensitive to the variation of angles of attack at all blade elements induced by neglecting the blade velocity than at $\theta_B = 0°$.

Even though the blade velocity has marginal impact on the amplitude of aerodynamic loads, it is essential to include it in the aerodynamic load calculations, since it plays an important role in terms of aerodynamic

damping. The blade motion is highly dominated by pendulum motion, for which the damping is small. Thus, the aerodynamic damping due to blade motion is crucial for the dynamic response of the blade. When it is neglected, the blade motion will be significantly overestimated.

6.3. Influence of tugger line arrangement on blade dynamic motion

As mentioned in Section 4, a representative value of the tugger line arm length 10 m (relative to the blade COG) was used, which is also shown in Fig. 18(a). To investigate the impact of tugger line arrangement on the dynamic characteristics of blade motion, a shorter tugger line arm length, i.e., 5 m was applied as illustrated in Fig. 18(b) for comparison. The results are shown in Fig. 19.

As shown in Fig. 19(a) and (b), the dynamic responses of blade sway and roll with tugger line arm length of 10 m are slightly smaller than that for the 5 m case. However, significant reduction of blade yaw motion is seen in Fig. 19(c) by increase of the tugger line arm length from 5 m to 10 m. That is because the tugger line arm length of 10 m increases the resonant frequency of blade yaw motion to a high level where resonant response is greatly reduced.

7. Results and discussions

The developed coupled simulation tool SIMO-Aero is applied to study the wind-induced dynamic response of the system prior to the mating process. The characteristics of stochastic dynamic response of the blade installation system is analyzed. The study is further extended by analyzing the extreme responses of the system under turbulent wind and extreme operating gust wind conditions.

7.1. Stochastic dynamic responses of the blade installation system in turbulent wind

The global responses of the blade installation system in load case LC2 are studied in this section. In load case LC3, the wind yaw angle ψ_W and blade initial pitch angle θ_B are both zero while the turbulence intensity T_I of the inflow wind varies from 1% to 15.72%.

Table 6 shows the mean values of the global responses, such as blade motions, aerodynamic loads on the blade and tensions in crane wire and tugger lines. The non-zero mean values of roll and yaw are respectively resulted from the aerodynamic roll and yaw moment. The roll motion leads to difference of tension in tugger lines, which causes the non-zero blade sway motion.

The standard deviations (STDs) of blade surge, heave and pitch are not presented since they are almost zero. The STDs of blade sway, roll and yaw with variation of wind turbulence intensity T_I are shown in Fig. 20(a). The blade roll motion is much larger than its yaw. As mentioned in Section 4, the tugger lines are deployed in the horizontal plane, which
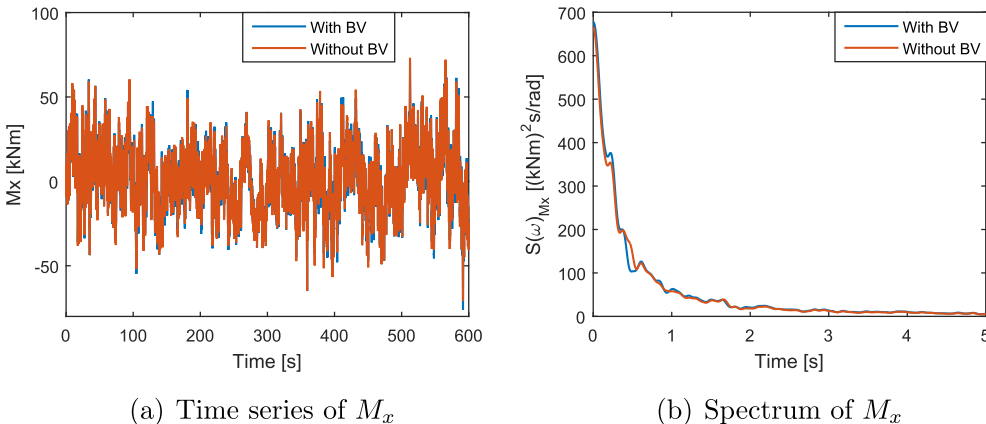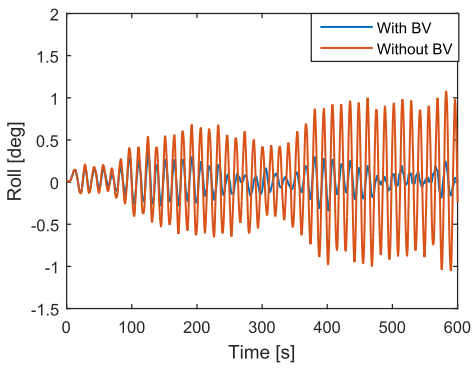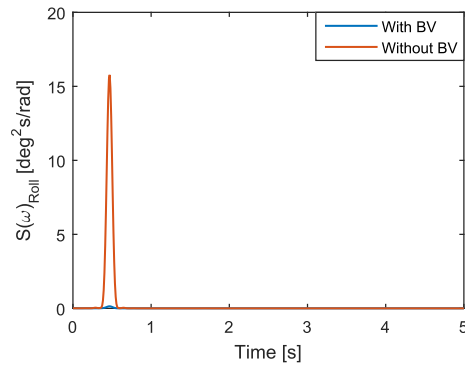

(a) Time series of M_x

(b) Spectrum of M_x

Fig. 14. Comparison of aerodynamic roll moment on the blade calculated based on the approach With and Without BV using load case LC2 with blade initial pitch angle $\theta_B = 0°$.

(a) Time series of blade roll motion

(b) Spectrum of blade roll motion

Fig. 15. Comparison of blade roll motion calculated based on approach With BV and Without BV using load case LC2 with blade initial pitch angle $\theta_B = 0°$.
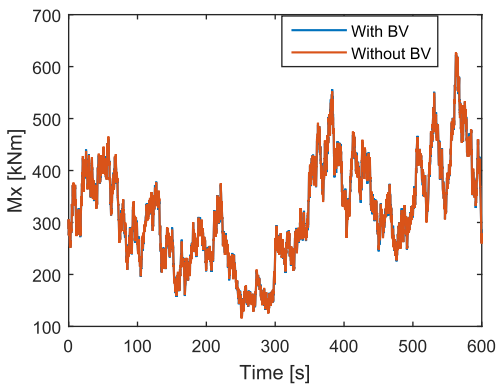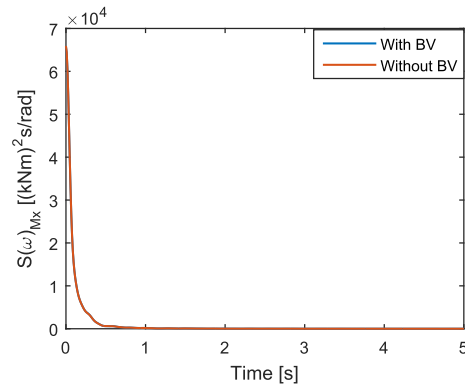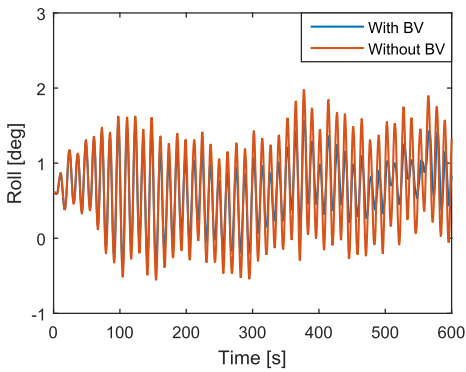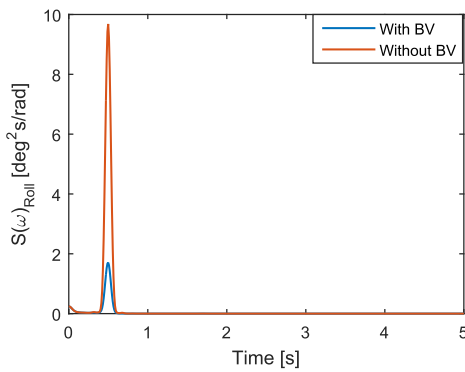

(a) Time series of M_x

(b) Spectrum of M_x

Fig. 16. Comparison of aerodynamic roll moment calculated based on approach With BV and Without BV using load case LC2 with blade initial pitch angle $\theta_B = 45°$.

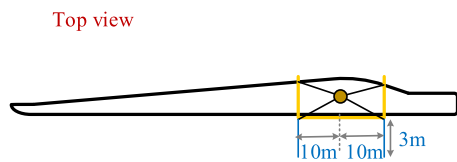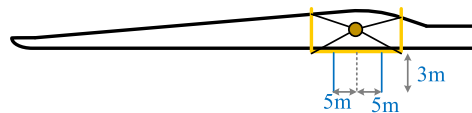(a) Time series of blade roll motion

(b) Spectrum of blade roll motion

Fig. 17. Comparison of blade roll motion calculated based on approach With BV and Without BV using load case LC2 with blade initial pitch angle $\theta_B = 45°$.

(a) Arm length 10m

(b) Arm length 5m

Fig. 18. Illustration of different tugger line arm length relative to blade COG.
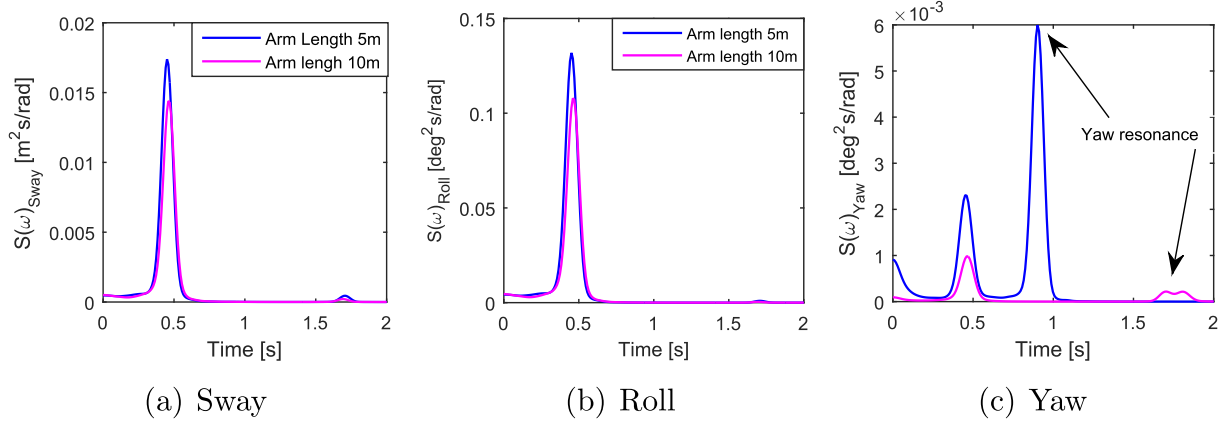
(a) Sway

(b) Roll

(c) Yaw

Fig. 19. Comparison of spectra of blade motions at its COG with different tugger line arm length in LC2 with blade initial pitch angle $\theta_B = 0°$.

Table 6
Mean value of global response in LC2.

	Parameter	Mean value	Unit
Blade motion	Surge	0.0016	[m]
	Sway	0.0046	[m]
	Heave	0.001	[m]
	Roll	0.014	[deg]
	Pitch	−0.0101	[deg]
	Yaw	0.0095	[deg]
Forces	F_x	2.145	[kN]
	F_z	5.5619	[kN]
	M_x	2.1596	[kNm]
	M_z	33.9096	[kNm]
	F_{cw}	965.4169	[kN]
	F_{tugg1}	21.0743	[kN]
	F_{tugg2}	24.4876	[kN]

Note: F_x and F_z– Aerodynamic drag and lift force; M_x and M_z– Aerodynamic roll and yaw moment; F_{cw}– Tension in the crane wire; F_{Tugg}– Tension in tugger lines.

control the blade yaw motion. However, constraints in the vertical plane are much weaker, leading to significant blade roll motion. Moreover, the STDs of blade sway, roll and yaw scale linearly with T_I. Besides, the STD variation of aerodynamic loads and tensions in crane wire and tugger lines, which are respectively shown in Fig. 20(b) ~ 20(d), experience a similar linear trend over T_I. The linear-scale relationship between system response and wind turbulence intensity can be expressed as:

$$\begin{bmatrix} \sigma_{sway} & \sigma_{roll} & \sigma_{yaw} \\ \sigma_{Fx} & 0 & \sigma_{Fz} \\ \sigma_{Mx} & 0 & \sigma_{Mz} \\ \sigma_{Fcw} & \sigma_{Ftug1} & \sigma_{Ftug2} \end{bmatrix} = T_I \mathbf{A} \tag{15}$$

where $\mathbf{A}$ is a matrix of the scale parameters, which are determined by the inflow wind characteristics and properties of the blade, such as mean wind speed, density of air, aerodynamic and structural properties of the blade, etc. This indicates that the STDs of blade motions, aerodynamic loads and wire tensions are proportional to the wind turbulent intensity. It agrees with and further extends one of the conclusions in Ref. (Gaunaa et al., 2014). The agreed conclusion is that the aerodynamic loading on a lifted blade is proportional to T_I. In LC2, $\mathbf{A}$ is found to be:

$$\mathbf{A} = \begin{bmatrix} 0.0026 & 0.0071 & 0.0008 \\ 0.0365 & 0 & 0.1029 \\ 1.1376 & 0 & 0.6176 \\ 0.1018 & 0.0842 & 0.0980 \end{bmatrix} \tag{16}$$

Furthermore, spectral analysis for blade motions is conducted, particularly for sway, roll and yaw motions. As shown in Fig. 21, all of the three spectra have a peak around $\omega = 0.46 rad/s$. The corresponding peak period is approximately 13.63s, which is the natural period of the 1st

mode of the system rigid body motion shown in Table 3. It indicates that the pendulum motion dominates the system responses. Besides, the yaw spectrum has other two small peaks between $\omega = 1.5 rad/s$ and $\omega = 2.0 rad/s$, which are respectively the eigen periods of the 7th and 8th modes shown in Table 3. Moreover, the spectrum peaks also increase with increasing turbulence intensity, which indicates that the blade motion is larger at higher turbulent intensity.

7.2. Stochastic motion response at blade root in turbulent wind

The blade root displacement relative to the hub position can be expressed as:

$$\begin{bmatrix} \Delta x & \Delta y & \Delta z \end{bmatrix}^T = \begin{bmatrix} x - x_0 & y - y_0 & z - z_0 \end{bmatrix}^T \tag{17}$$

where x_0, y_0 and z_0 are the position of hub center. Fig. 22 shows an example of the time series of blade root displacements and velocities. It is shown that the surge motion at blade root is the smallest while the heave motion is the largest. The horizontal tugger lines provide significant restoring in surge. However, the restoring in sway and heave relies on the slings and crane wires, which are quite limited.

Moreover, the spectral analysis for motions at blade root is conducted, as shown in Fig. 23. The heave spectrum at blade root, shown in Fig. 23(c) has the largest values, which is due to the significant blade roll motion. The surge spectrum at blade root in Fig. 23(a) has a similar trend with the blade yaw spectrum in Fig. 21(c). This indicates that the surge motion at blade root is mainly resulted from the blade yaw motion. The amplitude in sway spectrum at blade root in Fig. 23(b) is very close to the amplitude of blade sway spectrum in Fig. 21(a). It indicates that the blade rotational motions have marginal contribution to the sway motion at blade root, compared with blade sway.

7.3. Extreme response in turbulent wind

In this section, the extreme values of critical parameters in the lifting system during the blade mating process are studied. For the mating process of the blade onto hub, the blade root motion in the XZ plane is very critical. If the blade root motion in XZ plane is too large, the blade cannot be mated onto the hub. In this study, the blade root motion in the XZ plane is denoted as R_{root}:

$$R_{root} = \sqrt{(\Delta x)^2 + (\Delta z)^2} \tag{18}$$

The sway motion at blade root is also important because it might lead to destructive collisions. The sway motion at blade root is expressed as:

$$Y_{root} = \Delta y \tag{19}$$

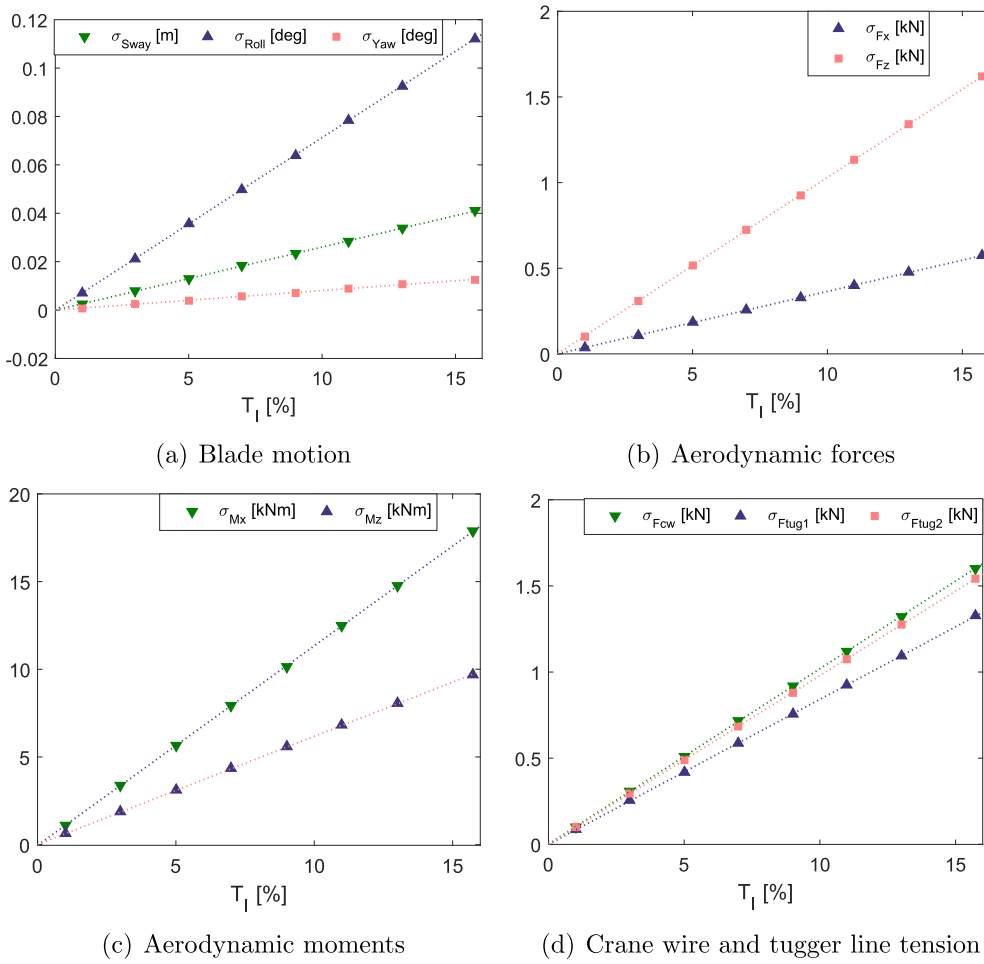Besides, the sway velocity at blade root is denoted as $V_{y,root}$.

Fig. 20. Standard deviation of aerodynamic loads on the blade in LC3: the dashed lines are the linearly fitted lines.

(a) Blade motion

(b) Aerodynamic forces

(c) Aerodynamic moments

(d) Crane wire and tugger line tension

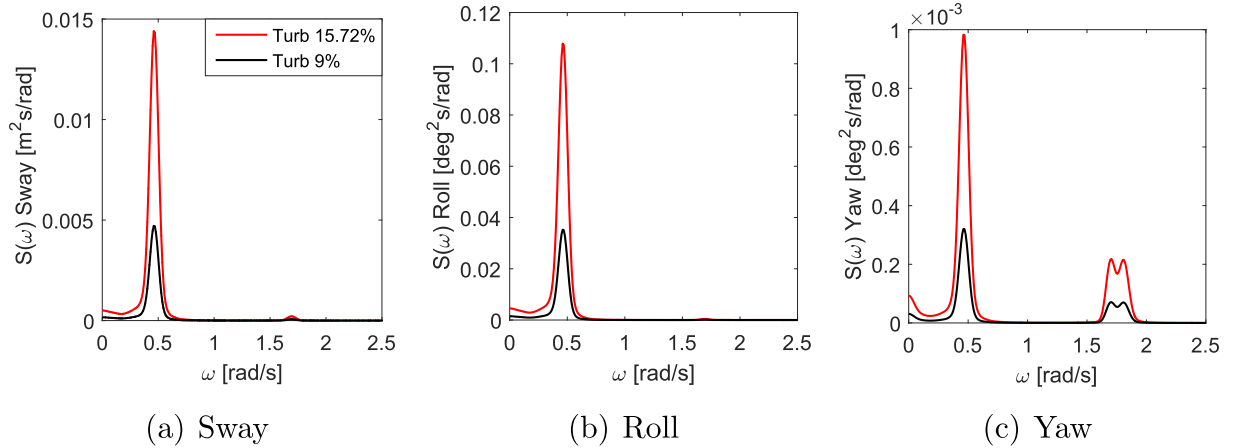
(a) Sway

(b) Roll

(c) Yaw

Fig. 21. Spectra of blade motions at its COG in LC3.

The tension in crane wire is not considered as a critical parameter since it has small variation from its mean value. The extreme tension in tugger lines F_{tug} is considered to be critical as it adds extra force and moment to the crane boom.

7.3.1. Extreme value estimation

The extreme values in this study are calculated based on the mean up-crossing rate method (Naess and Moan, 2012). In this method, it is assumed that the high threshold up-crossings are statistically independent, thus a Poisson probability distribution can be applied for the extreme values. Let $M(T) = max\{Y(t); 0 \le t \le T\}$ denotes the extreme value for a random process $Y(t)$ over the duration of T. If the process is stationary, the corresponding probability of exceedance for extreme values is given by:

$$P(M(T) > y) = 1 - exp\big(-\bar{v}^+(y)T\big) \qquad (20)$$

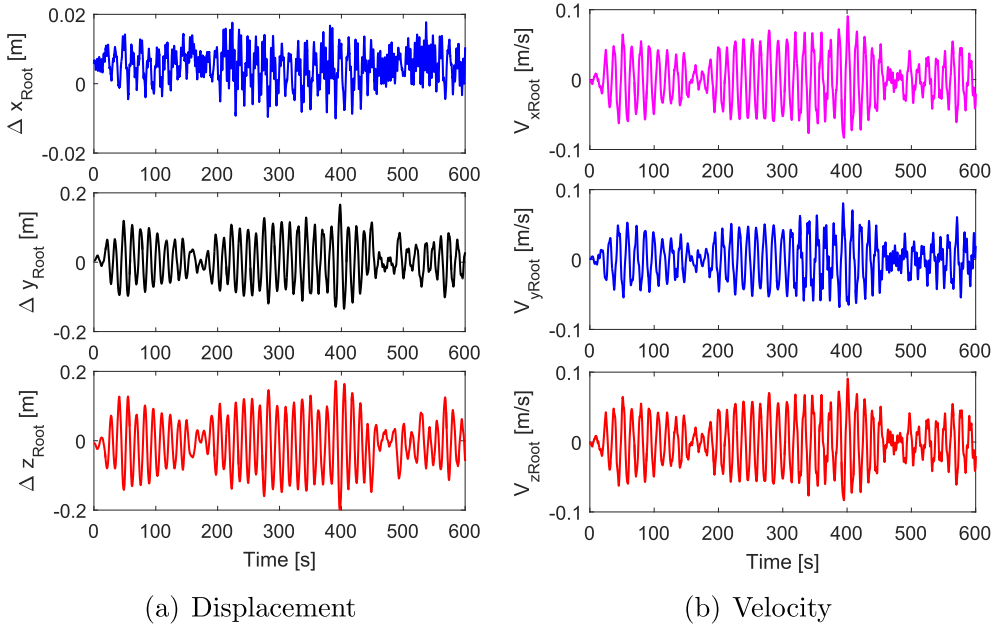where $\bar{v}^+(y)$ is the mean up-crossing rate. The sample-estimated mean

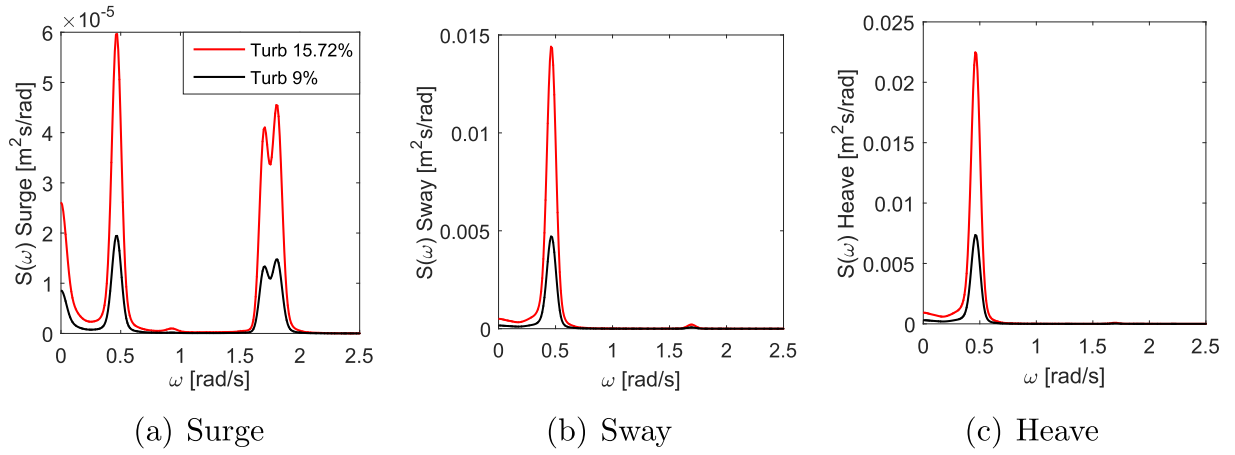**Fig. 22.** Example of time series for blade root displacement and velocity in LC3 with $T_I = 15.72\%$.

(a) Displacement

(b) Velocity

(a) Surge

(b) Sway

(c) Heave

Fig. 23. Spectra of motions at blade root in LC3.
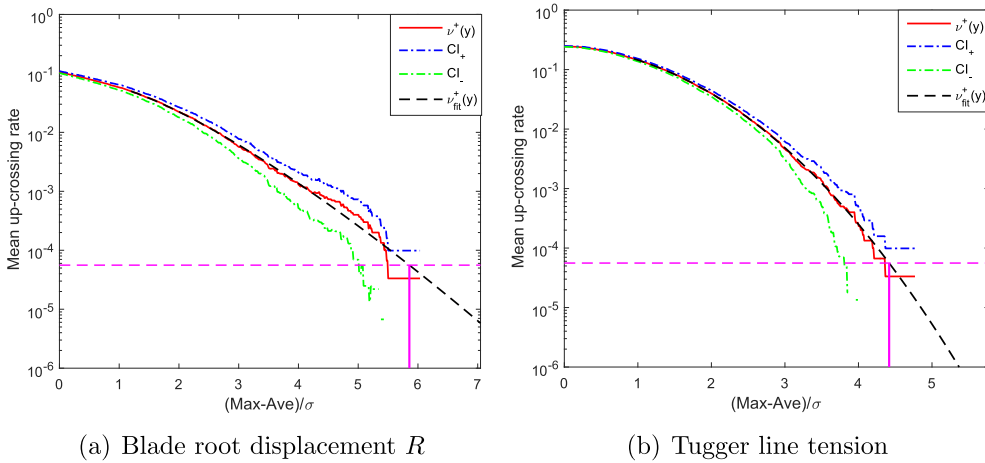
Fig. 24. Illustration of mean upcrossing rate extrapolation: LC3 with $T_I = 15.72\%$.

(a) Blade root displacement R

(b) Tugger line tension

value of $\bar{v}^+(y)$ can be calculated from simulated time series:

$$\widehat{\bar{v}}^+(y) = \frac{1}{kT} \sum_{j=1}^{k} n_j^+(y;T) \tag{21}$$

where $n_j^+(y;T)$ represents the number of up-crossings at level y of the *jth* time history during $[0 \quad T]$. Besides, k is the number of time series. With enough number of time series, a good approximation of 95% confidence interval (CI) can be obtained, i.e.:

$$CI_\pm(y) = \widehat{\bar{v}}^+(y) \pm \frac{1.96\widehat{s}(y)}{\sqrt{k}} \tag{22}$$

Eq.(21 ~ 22) are the basics for the empirical estimation of the mean upcrossing rate from direct numerical simulations, i.e., Monte Carlo simulation. However, direct numerical simulations are very time-consuming especially for low probability levels (Chai et al., 2015). To be more time-efficient, an extrapolation technique is applied (Naess and Gaidai, 2008).

The 10-min extreme values are studied with 3.3% probability of exceedence, which corresponds to occur once within 300min according to DNV-RP-H103 standard (Det Norske Veritas, 2011). The corresponding mean upcrossing rate is 5.593×10^{-5}. Fifty time series are used for the extreme value estimation of each sub-case. Fig. 24(a) and (b) present two examples of the fitting and extrapolation.

7.3.2. Effects of turbulence intensity

The influence of wind turbulence intensity T_I on the system extreme responses is studied in this section. Load cases LC3, LC4 and LC5 are used. The turbulence intensity T_I varies within each load case while the blade initial pitch angle θ_B increases from $0°$ in LC3 to $45°$ in LC5. Fig. 25 shows the results. Specifically, Fig. 25(a) shows the extremes of R_{root}. Fig. 25(b) and (c) present respectively the extreme sway displacement Y_{root} and velocity $V_{y,root}$ at blade root. Fig. 25(d) shows the extreme tension in tugger lines F_{tug}.

Similar to the standard deviations of the system response in Section 7.1, the system extreme responses also increase linearly with increasing T_I. At the same time, the extreme responses experience a non-linear increasing trend with the increase of θ_B. The extreme responses at $\theta_B = 0°$ is small. A dramatic increase occurs when θ_B increases to $30°$ in LC4. The extreme responses at $\theta_B = 45°$ in LC5 reach their respective peak values. The variation trend over θ_B is similar to that of the aerodynamic forces and moments shown in Figs. 10 and 11.

Take the extreme values of R_{root} as an example, the extreme value of R_{root} at $T_I = 15.72\%$ is over three times larger than the corresponding extreme at $T_I = 5\%$. Besides, the extreme value of R_{root} also varies a lot with increasing blade pitch angle. At $T_I = 15.72\%$, the extreme value of R_{root} increases over two times when θ_B increases from $0°$ to $45°$. Compared with R_{root}, the extreme value of Y_{root} is slightly smaller. At large pitch angle, the extreme value of $V_{y,root}$ is significant. This indicates that large blade pitch angle makes it more difficult to mate the blade onto hub and increases the chance of blade root collision with hub.
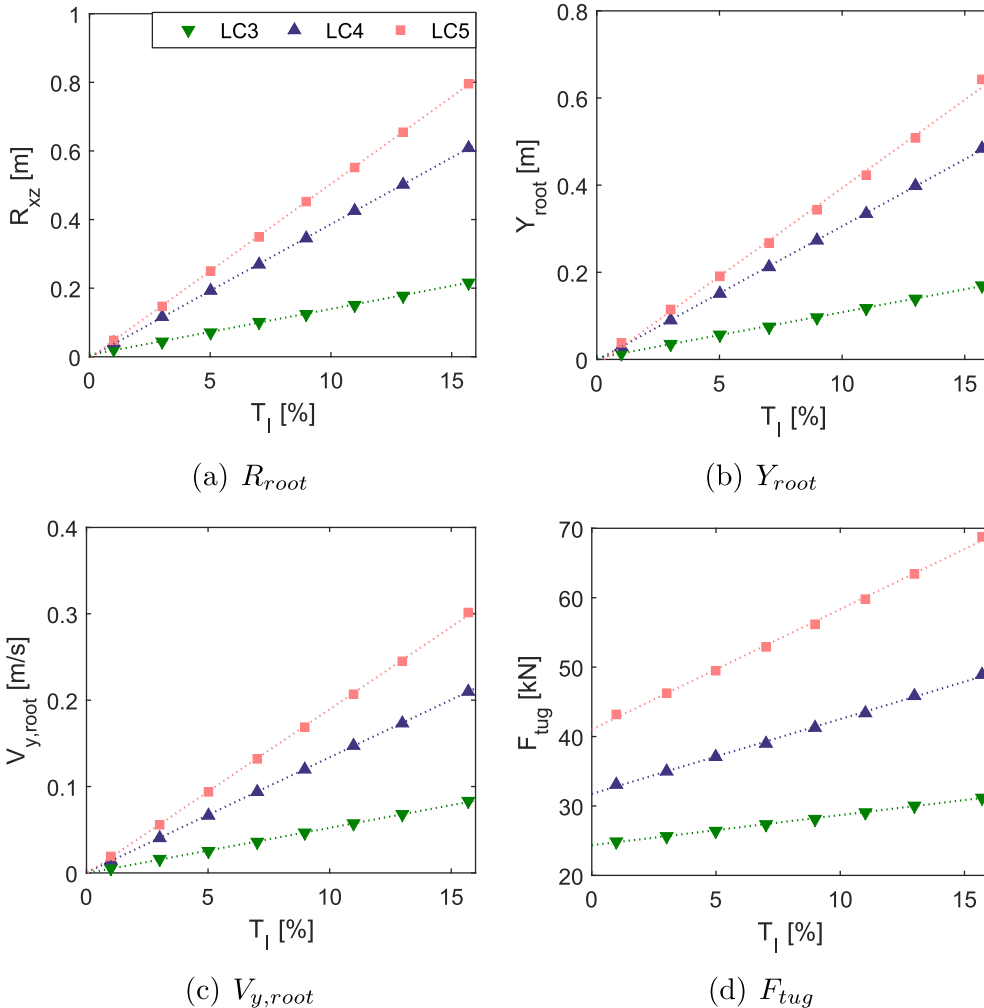

Fig. 25. Extreme responses of blade root motion and tension in tugger lines in LC3 ∼ LC5: the dashed lines are the linearly fitted lines.
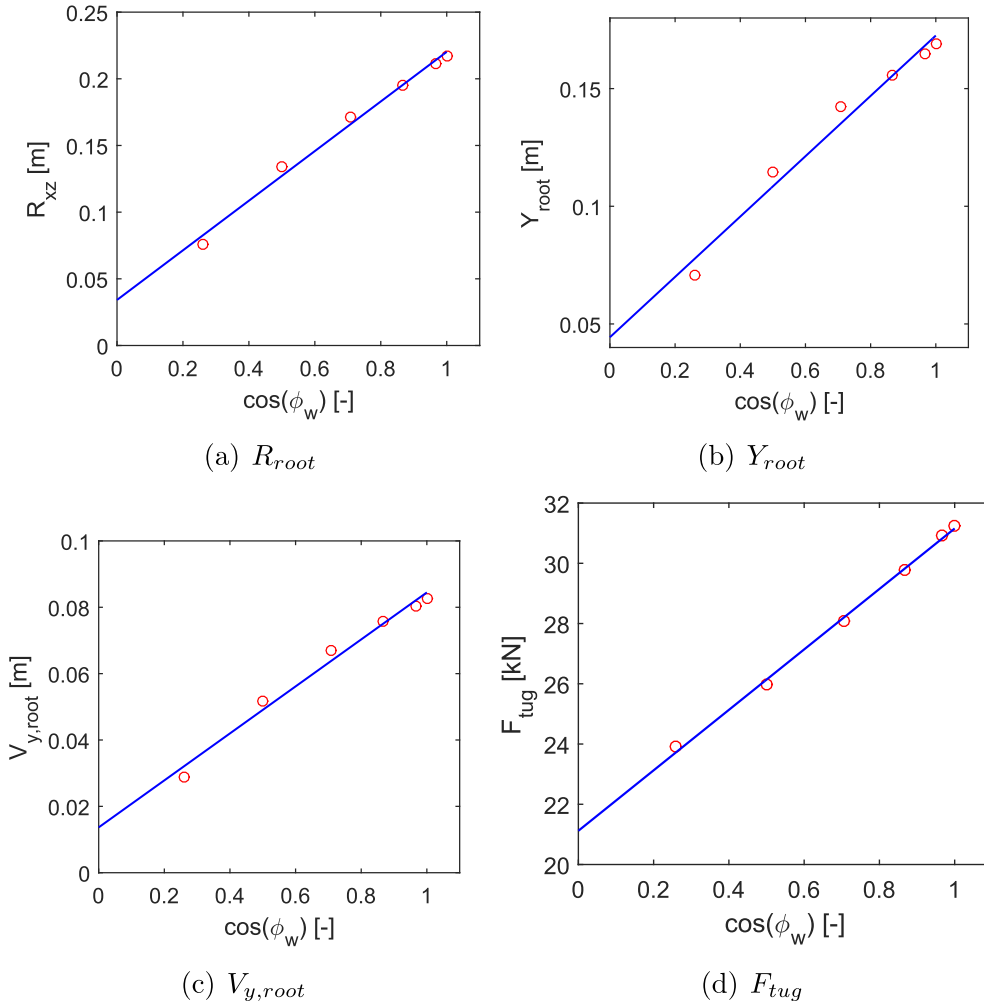
(a) R_{root}

(b) Y_{root}

(c) $V_{y,root}$

(d) F_{tug}

(a) R_{root}

(b) Y_{root}

(c) $V_{y,root}$

(d) F_{tug}

Fig. 26. Extreme root displacement and tugger line tension in LC6.

7.3.3. Effects of wind direction

Fig. 26(a) shows the influence of wind yaw angle ψ_B on the extreme responses of the system using load case LC6. Six yaw angles are simulated, varying between $0°$ and $75°$.

It is shown that all the extreme responses are linear functions of the cosine functions of ψ_B. The fitted line is presented as the blue curve in Fig. 26(a). It is shown that the system extreme responses decrease with increasing wind yaw angle. This indicates that larger wind yaw angle makes the mating operation of a blade onto hub easier.

7.4. Stochastic dynamic response of the system in extreme operating gust wind

The influence of extreme operating wind gust on the dynamic response of the system is studied in this section, as shown in Fig. 27. Different blade initial pitch angles θ_B are applied, i.e. $0°$ in LC7 and $45°$ in LC8. The same gust wind is used for both cases. The gust wind inflow angle ψ_B is zero and the mean wind speed is 10 m/s. Fig. 27(b) shows the time series of the gust wind speed. The wind gust starts at 300s and ends at 310.5s. The other graphs in Fig. 27 show the blade root motion and aerodynamic loading on the blade. To have a better illustration of the response, time series between 290s and 350 is presented.

As shown in Fig. 27(b) and (c), the aerodynamic loads on the blade follow the gust wind simultaneously. Compared with LC7, the aerodynamic loads in LC8 have a much larger peak. Nevertheless, the aerodynamic loads in both cases become stable after the gust wind ends, which indicates that the aerodynamic loads on a lifted blade are mainly dominated by inflow wind velocity.

However, compared with the blade aerodynamic loads, the motion responses at blade root experience a different trend. As shown in Fig. 27(d) ~ 27(f), the blade root motions fluctuate a lot. Moreover, much larger fluctuations are seen by blade root motion in LC8. The fluctuation of blade root surge motion (Δx) is dominated by two cycles, which agrees with the spectrum of blade root surge motion in Fig. 23(a). Apparently, the sway (Δy) and heave (Δz) motions at blade root fluctuate with the natural frequency of the 1st eigen mode shown in Fig. 23(b) and (c).

The maximum responses of blade root motions are listed in Table 7. In load case LC7, the maximum values of R_{root}, Y_{root} and $V_{y,root}$ are all very small. Nevertheless, in LC8, the maximum values of R_{root} and Y_{root} are respectively 0.43 m and 0.33 m. Compared with results in Fig. 25, the maximum responses in the extreme operating gust wind are equivalent to the extreme responses under turbulent wind with turbulence intensity of 7%.

8. Conclusions

This paper deals with the development, verification and application of an integrated simulation tool for modeling and dynamic analysis of single blade installation for wind turbines. On the basis of cross-flow principle, an aerodynamic code denoted as Aero code is developed considering the effect of wind turbulence, extreme operating gusts and dynamic stall. The developed Aero code is then coupled with SIMO to formulate the integrated simulation tool, i.e., SIMO-Aero code. The coupled SIMO-Aero code could be used to evaluate the system
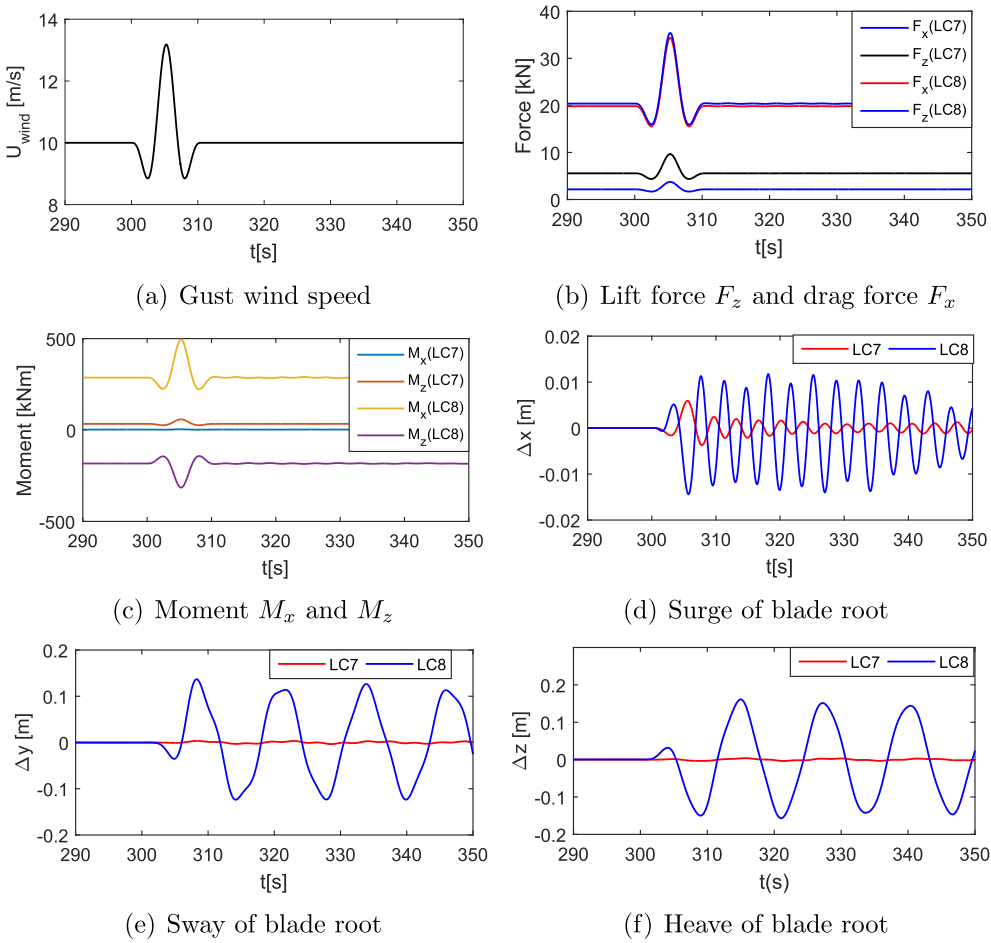
(a) Gust wind speed

(b) Lift force F_z and drag force F_x

(c) Moment M_x and M_z

(d) Surge of blade root

(e) Sway of blade root

(f) Heave of blade root

Fig. 27. Blade root motion and blade aerodynamic loads in LC7 and LC8.

Table 7
Maximum responses of blade root motion in LC7 and LC8.

Parameter	Maximum		Unit
	LC7	LC8	
R_{root}	0.0060	0.4257	[m]
Y_{root}	0.0034	0.3308	[m]
$V_{y,root}$	0.0030	0.0852	[m/s]

performance during single blade installation for offshore as well as onshore wind turbines, accounting for aerodynamics, hydrodynamics and wire coupling mechanics.

Verification of the simulation tool is conducted module by module. SIMO has been widely verified and used. The Aero code is verified by code-to-code comparisons against HAWC2 results. It is shown that the Aero code gives accurate estimation of the aerodynamic loads. The characteristics of aerodynamic loads on a lifted blade are quite different from a rotating one. For a lifted blade, the main contributions of aerodynamic loads come from the middle and root part of the blade. Furthermore, the aerodynamic damping is of great importance in the dynamic response of blade during installation.

The developed integrated simulation tool is then applied to simulate the wind-induced dynamic responses of a DTU 10MW reference wind turbine blade prior to mating using a jack-up crane vessel. Stochastic dynamic analysis reveals the characteristics of the blade installation system. The blade motions are dominated by pendulum motions. Sway and roll motion of the blade are significant, leading to large sway and heave motion at the blade root. Furthermore, the system critical responses are identified, which are respectively blade root surge and heave motion, displacement and velocity of root sway and tension in tugger

lines. Moreover, the critical responses are further studied in turbulent wind and gust wind. The results indicate that a larger wind yaw angle and a smaller blade pitch angle ease the difficulty of mating the blade onto the hub. Besides, installing a blade under extreme operating gust wind is less difficult than in strong turbulent wind.

The horizontally deployed tugger lines are commonly used in offshore blade installation. However, they do not provide enough constraints in the lateral and vertical directions, leading to significant blade root motions in sway and heave. To reduce motions at blade root, increasing damping in the tugger lines or adjusting tugger line configurations might help. Besides, a yoke with automatic motion compensation is expected to have a better control of motions at the blade root.

Moreover, the blade root motion is highly sensitive to the initial pitch angle of the blade, wind turbulence intensity and wind direction. During the planning and operational phases of offshore wind turbine blade installation, these factors are recommended to be considered together with the mean wind speed. In this way, the offshore blade installation could be conducted safely, economically and more efficiently.

9. Future work

In this study, the jack-up crane vessel including the crane were assumed to be rigid and rigidly fixed to the seabed. In reality, the crane tip of the jack-up crane vessel moves due to the motion of the jack-up vessel under wave loads and the deformation of the crane at large lifting height. This movement has some impacts on the dynamic response of the blade during installation. A future study will be conducted to evaluate the influence of wave-induced loads on the jack-up crane vessel and deformation of the jack-up crane vessel and the crane on the dynamic behavior of the blade during installation.

Study on blade installation by a floating crane vessel is also to be conducted by using the developed simulation tool in the future. It is expected to be favored by the offshore wind industry, due to the rapid development of offshore wind energy.

Acknowledgment

References

Ahn, D., Shin, S.-C., Kim, S.-Y., Kharoufi, H., Kim, H.-C., 2017. Comparative evaluation of different offshore wind turbine installation vessels for Korean west–south wind farm. International Journal of Naval Architecture and Ocean Engineering 9 (1), 45–54.

Bak, C., Zahle, F., Bitsche, R., Kim, T., Yde, A., Henriksen, L.C., Hansen, M.H., Natarajan, A., 2013. Description of the DTU 10 MW Reference Wind Turbine. Tech. Rep. DTU Wind Energy Report-I-0092. Technical University of Denmark.

Chai, W., Naess, A., Leira, B.J., 2015. Stochastic dynamic analysis and reliability of a vessel rolling in random beam seas. J. Ship Res. 59 (2), 113–131.

Cheng, Z., Madsen, H.A., Gao, Z., Moan, T., 2016. Aerodynamic modeling of floating vertical axis wind turbines using the actuator cylinder flow method. Energy Procedia 94, 531–543.

Cheng, Z., Madsen, H.A., Gao, Z., Moan, T., 2017. A fully coupled method for numerical modeling and dynamic analysis of floating vertical axis wind turbines. Renew. Energy 107, 604–619.

Det Norske Veritas, 2011. Modelling and Analysis of Marine Operations, Standard DNV-RP-H103.

DONG energy, 2016. Burbo Bank Extension. http://www.dongenergy.co.uk/uk-business-activities/wind-power/operational-offshore-wind-farms. (Accessed 24 October 2017).

Gaunaa, M., Bergami, L., Guntur, S., Zahle, F., 2014. First-order aerodynamic and aeroelastic behavior of a single-blade installation setup. J. Phys. Conf. 524 (1), 012073.

Gaunaa, M., Heinz, J., Skrzypiński, W., 2016. Toward an engineering model for the aerodynamic forces acting on wind turbine blades in quasisteady standstill and blade installation situations. J. Phys. Conf. 753 (2), 022007.

GL Garrad Hassan, 2010. Bladed Theory Manual, version 4.0. .

Global Wind Energy Council, 2017. Global Wind Statistics 2016.

Gupta, S., Leishman, J.G., 2006. Dynamic stall modelling of the S809 aerofoil and comparison with experiments. Wind Energy 9 (6), 521–547.

NV High Wind, 2015. Boom Lock. http://www.high-wind.eu/boomlock/. (Accessed 1 September 2017).

Hoerner, S.F., Borst, H.V., 1985. Fluid-dynamic Lift: Practical Information on Aerodynamic and Hydrodynamic Lift. Hoerner Fluid Dynamics, Vancouver, WA.

Horner, S., 1965. Fluid Dynamic Drag: Practical Information on Aerodynamic Drag and Hydrodynamic Resistance. Hoerner Fluid Dyn., Midland Park, NJ.

IEC, 2005. International Standard 61400-1, Wind Turbines, Part 1: Design Requirements.

IEC, 2009. IEC 61400-3, Wind Turbines, Part 3: Design Requirements for Offshore Wind Turbines.

Jonkman, B.J., 2009. Turbsim User's Guide, Version 1.50. .

Kuijken, L., 2015. Single Blade Installation for Large Wind Turbines in Extreme Wind Conditions. Master thesis. Technical University of Denmark.

Kvittem, M.I., Bachynski, E.E., Moan, T., 2012. Effects of hydrodynamic modelling in fully coupled simulations of a semi-submersible wind turbine. Energy Procedia 24, 351–362.

Lankhorst ropes, 2013. Offshore steel wire ropes. http://www.lankhorstropes.com/files/uploads/Offshore/brochures/Steel_Wire_Rope_brochure_100dpi_April_2013.pdf. (Accessed 13 February 2017).

Larsen, T.J., Hansen, A.M., 2015. How 2 HAWC2, the User's Manual, Version 12.2. User Manual. Risø National Laboratory, DTU, version 12.2. .

Leishman, J.G., Beddoes, T., 1989. A semi-empirical model for dynamic stall. J. Am. Helicopter Soc. 34 (3), 3–17.

Liftra, 2012. Blade Dragon. http://www.liftra.com/product/product-2/. (Accessed 1 September 2017).

MARINTEK, 2015a. Simo-theory Manual, version 4.6. .

MARINTEK, 2015b. Simo-user Manual, version 4.4.1. .

Naess, A., Gaidai, O., 2008. Monte Carlo methods for estimating the extreme response of dynamical systems. J. Eng. Mech. 134 (8), 628–636.

Naess, A., Moan, T., 2012. Stochastic Dynamics of Marine Structures. Cambridge University Press, Cambridge, UK.

Siemens, 2014a. Innovative Yoke for Safe Wind Turbine Blade Lifting. http://www.offshorewind.biz/2014/06/26/innovative-yoke-for-safe-wind-turbine-blade-lifting/. (Accessed 1 September 2017).

Siemens, 2014b. Siemens Wind Turbine Blade Being Positioned. https://www.siemens.co.uk/en/news_press/index/news_archive/2014/major-uk-offshore-wind-manufacturing-site-to-be-built-by-siemens.htm. (Accessed 1 September 2017).

Uraz, E., 2011. Offshore Wind Turbine Transportation & Installation Analyses Planning Optimal Marine Operations for Offshore Wind Projects. Master thesis. Gotland University.

Wang, Y., He, W., Tian, D., 2012. Calculation of hoisting forces of the wind turbine rotor based on wind conditions. Renew. Energy 39 (1), 323–328.

Wang, Y., Tian, D., He, W., 2014. Computation of hoisting forces on wind turbine blades using computation fluid dynamics. Appl. Mech. Mater. 446, 452–457.